



Strain-gradient induced topological transition in bent nanoribbons of the Dirac semimetal Cd₃As₂Wen-Zhuang Zheng, Tong-Yang Zhao, An-Qi Wang,^{*} Dai-Yao Xu, Peng-Zhan Xiang ,
Xing-Guo Ye, and Zhi-Min Liao [†]*State Key Laboratory for Mesoscopic Physics and Frontiers Science Center for Nano-optoelectronics,
School of Physics, Peking University, Beijing 100871, China*

(Received 22 July 2021; accepted 12 October 2021; published 22 October 2021)

Dirac semimetal is an ideal parent state to realize various exotic states of matter, such as quantum spin Hall state, Weyl semimetal phase, and Majorana zero modes. Topological phase transition allows for the switching between these different topological states. Here, in this paper, we exhibit experimentally an effective approach of inducing topological phase transition in Cd₃As₂ nanoribbons by applying a bending strain profile onto the sample. The local strain varies linearly from compression to tension through the cross-section of a bent nanoribbon. The strain gradient causes obvious lattice deformation and breaks the C_4 rotational symmetry, thus opening an energy gap at the Dirac points and making the bulk gapful. When further increasing the strain strength, the local strain effect dominates over the symmetry-breaking effect, where spatially-varying band shift becomes prominent across the nanoribbon. Our results demonstrate the effect of strain gradient on the evolution of energy band structures, which should be valuable for further study of strain-mediated topological phase transition.

DOI: [10.1103/PhysRevB.104.155140](https://doi.org/10.1103/PhysRevB.104.155140)**I. INTRODUCTION**

The combination of topology and physics has ushered a variety of quantum materials, such as topological insulators [1,2], Dirac semimetals [3–6], Weyl semimetals [3–6], and topological superconductors [1]. Topological Dirac semimetals (TDSs), featured with gapless Dirac cones in the bulk band structure, are of vital importance as a parent state of various other topological phases. For instance, reducing the material thickness would possibly trigger a phase transition from TDSs to topological insulators [7,8]. The quantum confinement effect in an ultrathin TDS film would lead to a crossover to a two-dimensional topological insulator, with the emergence of a quantum spin Hall state [8,9]. Upon breaking the time-reversal symmetry via external magnetic field or magnetic exchange interaction, the original Dirac cone would split into Weyl cones, accompanied by the presence of a magnetic Weyl semimetal phase [3–6]. Additionally, when proximitized with s -wave superconductors, a TDS is proposed to support the topological superconducting phase and Majorana zero modes [10–13], which are significant for implementation of topological qubit and fault-tolerant quantum computation. A TDS provides an ideal platform to study the phase transition between different quantum states, which is valuable for fundamental and application-based studies and has attracted current research interest.

As a prototypical TDS, Cd₃As₂ has two gapless Dirac cones along the k_z direction protected by the C_4 rotational symmetry [8]. Pristine Cd₃As₂ has demonstrated abundant features, including chiral anomaly [14], π Aharonov-Bohm

oscillations [15,16], quantum Hall effect [9,17,18], and spin-polarized Fermi arc surface states [19–21]. In previous literature on topological phase transitions in Cd₃As₂, widely acknowledged useful methods include introducing interplay with external electromagnetic fields [22–24] or reducing sample dimensions to introduce the quantum confinement effect [8,9]. Experimental works have demonstrated feasibility of magnetic field-driven topological phase transition in Cd₃As₂ into Weyl semimetals, quantum Hall insulators, or trivial insulators [9,14,17,18,25,26], and predictions that Dirac semimetal Cd₃As₂ can turn into a 2D topological insulator in an ultrathin film are also proposed [8]. Recently, an emergent type of mechanism that induces topological phase transitions in topological semimetals has been proposed, that is, introducing certain strain profiles onto the whole lattice [27–30]. Rather than introducing external electromagnetic fields or reducing the sample thickness, the strain-induced band modulation can be easily achieved during sample fabrication, which is more static and intrinsic as a sample property and more intuitive in the symmetry analysis. The correlation between strain profile and gauge field theories further enriches the physical implication of relevant topological phase transitions [31–34].

In this paper, we demonstrate the variation of electronic properties modulated by static bending strain applied on Cd₃As₂ nanoribbon devices through transport experiments. Compared with the case of straight nanoribbons, the bent nanoribbon displays some distinct features, i.e., a second turning point in the ρ - T curve and flat region in the ρ - V_g curve. This can be well understood by considering that the introduced strain gradient breaks the pristine lattice symmetry and opens a global bulk gap near the neutrality point. When further increasing the bending strength applied to the nanoribbon, the local strain-induced energy band shift dominates and renders the bulk gap closing.

^{*}anqi0112@pku.edu.cn[†]liaozm@pku.edu.cn

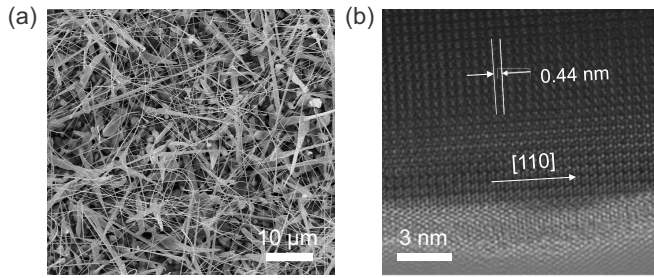


FIG. 1. Characterization of the synthesized Cd_3As_2 nanoribbons. (a) Scanning electron microscopy (SEM) image of the as-grown Cd_3As_2 nanoribbons, demonstrating great flexibility. (b) High-resolution transmission electron microscopy (TEM) image of a typical nanoribbon with interplanar spacing ~ 0.44 nm, indicating the $[110]$ growth orientation.

II. METHODS

Cd_3As_2 nanoribbons were grown by the chemical vapor deposition method, as reported in our previous work [35]. Cd_3As_2 nanostructures with a typical scale of several tens of microns in length and several hundreds of nanometers in diameter were obtained and examined using scanning electron microscopy (SEM), as shown in Fig. 1(a). The nanoribbons show excellent mechanical flexibility, allowing us to investigate the effect of the bending profile on them without introducing fractures to the samples. The high-resolution transmission electron microscopy (TEM) image shows the nanoribbon has an interplanar spacing of ~ 0.44 nm, indicating the $[110]$ growth orientation [Fig. 1(b)]. In this paper, the selected nanoribbons have a thickness ranging from 170 to 200 nm. During device fabrication, the nanoribbon was first transferred onto the Si/SiO_2 substrate, and an in-plane bending profile was then introduced mechanically under an optical microscope using a glass tip. To help consolidate the bending shape of the nanoribbon, a 3-nm-thick Al_2O_3 layer was deposited on the whole sample using the atomic layer deposition system. Standard electron beam lithography and electron beam evaporation techniques were adopted to fabricate Ti/Au electrodes on regions of nanoribbons with variant bending curvatures. We have experimentally investigated a total of 12 bent nanoribbon devices, in which the results are consistent with each other. In the following, we mainly elaborate on three typical devices, marked as device A, B, and C (see Appendix A).

Figure 2(a) shows the SEM image of a bent Cd_3As_2 nanoribbon device. In such a bent nanoribbon, lattice deformation and strain mainly happen along the axial direction of the ribbon. The strain u varies linearly from tension (outside the ribbon) to compression (inside the ribbon) across a strain-neutral plane (geometrical middle plane of the ribbon), leading to a strain gradient along the radial direction [Fig. 2(b)]. The value of the strain gradient is $g = 1/r$, where r is the local curvature radius. Then the maximum values of tensile and compressive strain at the outer and inner side can be estimated by $\varepsilon = \pm \frac{d}{2r}$, where d is the width of the nanoribbon, as illustrated in the top view in Fig. 2(b).

From the above perspective, the lattice deformation varies spatially in a continuous manner, making the system a com-

plex “parallel” configuration of many local lattice structures. Thus, theoretical analysis of band evolution is necessary here to shed light on the transition of transport properties in a bent nanoribbon, serving as guidance for experimental exploration. The topological semimetal nature of unbent Cd_3As_2 arises from the inverted bands due to strong spin-orbit coupling [8], as depicted in Fig. 2(c). The strength of coupling, as well as all the hopping amplitudes in the system, should be functions of lattice parameters. Therefore, the strain profiles applied on Cd_3As_2 nanoribbons in our experiment generate corrections to local lattice parameters and directly change the low-energy band structures. By unidirectionally increasing or decreasing certain lattice parameters, the conduction and valence band shall move accordingly, as indicated by relevant density functional theory calculations [36,37], toward a lower or higher energy. In the case of a weak bending profile, a considerable energy gap induced by the breaking of C_4 rotational symmetry shall emerge [8,25,37,38], while the overall energy shifts of bands remain sufficiently small. There may exist a global energy gap in the whole sample, and the system would exhibit insulating behavior when the Fermi level is tuned into the global gap [Fig. 2(d)]. In the strongly bending case, however, the shift of the energy band becomes more significant, and no universal gap for the whole sample exists [Fig. 2(e)]. Thus, the Fermi level always intersects with energy bands, and the corresponding transport measurements manifest a p - to n -type crossover in one single device. We believe that the bending gradient g , which determines the size of the gap induced by symmetry reduction, and the sample width d , which relates to the maximal band shift, together decide the final energy band structure of the system.

III. RESULTS AND DISCUSSION

The results discussed in the main text all come from device A. Transport measurements were performed in three different bent regions of device A, i.e., region A1, A2, and A3 (see Appendix B). We firstly investigate on the bent region A1 [denoted by the red arrow in Fig. 2(a)]. The local curvature radius r and width d of the bent region are $4.13 \mu\text{m}$ and 199 nm, respectively, corresponding to a maximal strain amplitude $\varepsilon = 2.41\%$. The ρ - T curve corresponding to A1 is plotted in Fig. 3(a). The ρ - T curve exhibits a clear insulating behavior in the high-temperature region, where resistivity ρ increases monotonically with decreasing T . This kind of insulating behavior of ρ - T curves in the high-temperature region has been observed in several semimetallic systems with high sample quality, including Cd_3As_2 (Ref. [39]) and ZrTe_5 (Ref. [40]), for instance. The more noteworthy feature is the second turning point which emerges at a low temperature of ~ 10 K [see inset of Fig. 3(a)]. In previous reports on ρ - T curves of topological semimetals, the resistivity increases to only one single maximum with decreasing temperature, then drops monotonically until the temperature approaches 0 K. In our result, the emergent second turning point at 10 K is a very distinctive phenomenon and has implication on possible phase transitions occurring in the bent Cd_3As_2 nanoribbon. Specifically, the insulating ρ - T behavior < 10 K may indicate the opening of a bulk gap in the energy band structure. Metal-insulator transitions have been confirmed from ρ - T spectra in many systems

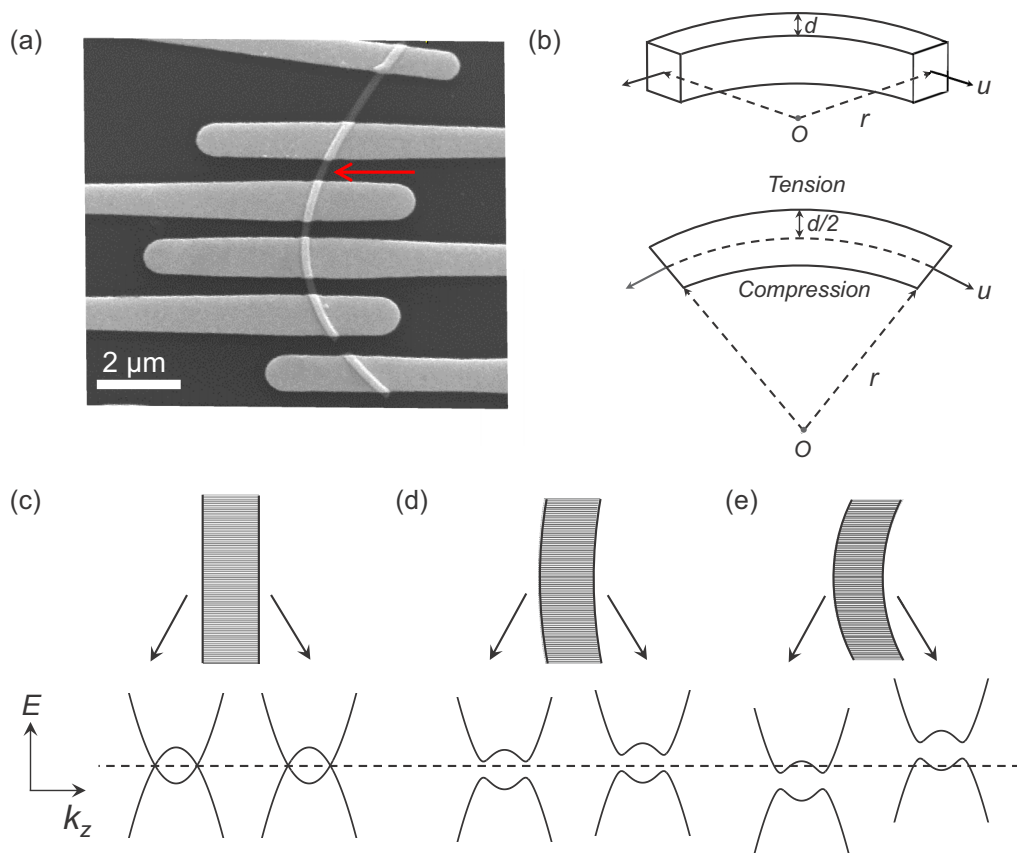


FIG. 2. Schematic of bending strain profiles and corresponding band structures. (a) Scanning electron microscopy (SEM) image of the bent nanoribbon device A. The red arrow indicates the position A1 (local curvature radius $r = 4.13 \mu\text{m}$, strain gradient $g = 24.2\% \mu\text{m}^{-1}$) for transport measurements in Fig. 3. (b) Schematic illustration of the bending strain acting on the Cd_3As_2 nanoribbon. The strain u along the axial [110] direction changes from tension (outside the ribbon) to compression (inside the ribbon) across a strain-neutral plane (geometrical middle plane of ribbon). The nanoribbon width and radius of curvature are marked as d and r , respectively. (c)–(e) Schematic of bulk band structure evolution in the bent Cd_3As_2 nanoribbon as the bending strength increases. Quantum confinement is ignored here for simplicity. (c) Case of the straight nanoribbon. Cd_3As_2 has two gapless Dirac cones along the k_z direction protected by the C_4 rotational symmetry. Absence of strain ensures the band structure on both sides of the sample is identical. (d) Case of weak bending strain. On the one hand, the strain gradient reduces lattice symmetry and opens a bulk gap, resulting in the ω shape of the local band structure. On the other hand, local strain modifies lattice parameters, which further induces slight energy shift in conduction and valence bands. (e) Case of strong bending strain. With the band shifts further, the system will enter an “indirect gapless” regime, and the Fermi level will always intersect with conduction or valence bands.

[41–47]. We also performed measurements on gate voltage dependence of the resistivity in the bent region, as shown in Fig. 3(b). Compared with the standard ρ - V_g curves obtained in the straight Cd_3As_2 nanowires [48], a conspicuously different feature can be observed here that the resistivity maximum no longer exhibits a single peak line shape but rather a plateaulike flat region, with plateau width ~ 20 V. The stable maximal resistivity value over a relatively wide range of gate voltages is consistent with the scenario of an energy gap in the bulk band structure [49–51]. Once the Fermi level is tuned into the gap, the bulk conduction is greatly suppressed, and the overall conduction becomes dominated by other mechanisms, including disorders and surface states [52–54], which are little affected by gate voltage. Therefore, a relatively flat region between n - and p -type conduction in the ρ - V_g curve is experimentally observed here. In contrast, for an ideal Dirac semimetal system, the gapless band structure results in a sharp transition between n - and p -type conduction, and the

resistivity near the Dirac point should therefore take the form of a narrow peak. Electron and hole mobilities can also be extracted from the ρ - V_g curve, which take the values $\mu_e = 1.59 \times 10^4 \text{ cm}^2/(\text{V} \cdot \text{s})$ and $\mu_h = 3.81 \times 10^2 \text{ cm}^2/(\text{V} \cdot \text{s})$, obviously reduced from the typical values in high-quality Cd_3As_2 nanostructures [55]. The flat region in our ρ - V_g curve, as well as the reduced mobility, thus reveals from a parallel aspect the breakdown of the Dirac cone structure in the bent nanoribbon.

To better reveal the topological transition occurring in the bent nanoribbon, we also performed magnetotransport measurements on the bent region under an out-of-plane magnetic field B . Figure 3(c) shows the resistivity variation $\Delta\rho$ as a function of $1/B$ in the bent region A1. The oscillatory pattern here is reminiscent of Shubnikov–de Haas (SdH) oscillation, which emerges from quantized Landau levels under high magnetic field. In our result, the oscillation seemingly exhibits a periodic behavior under high magnetic field $B > 5$ T

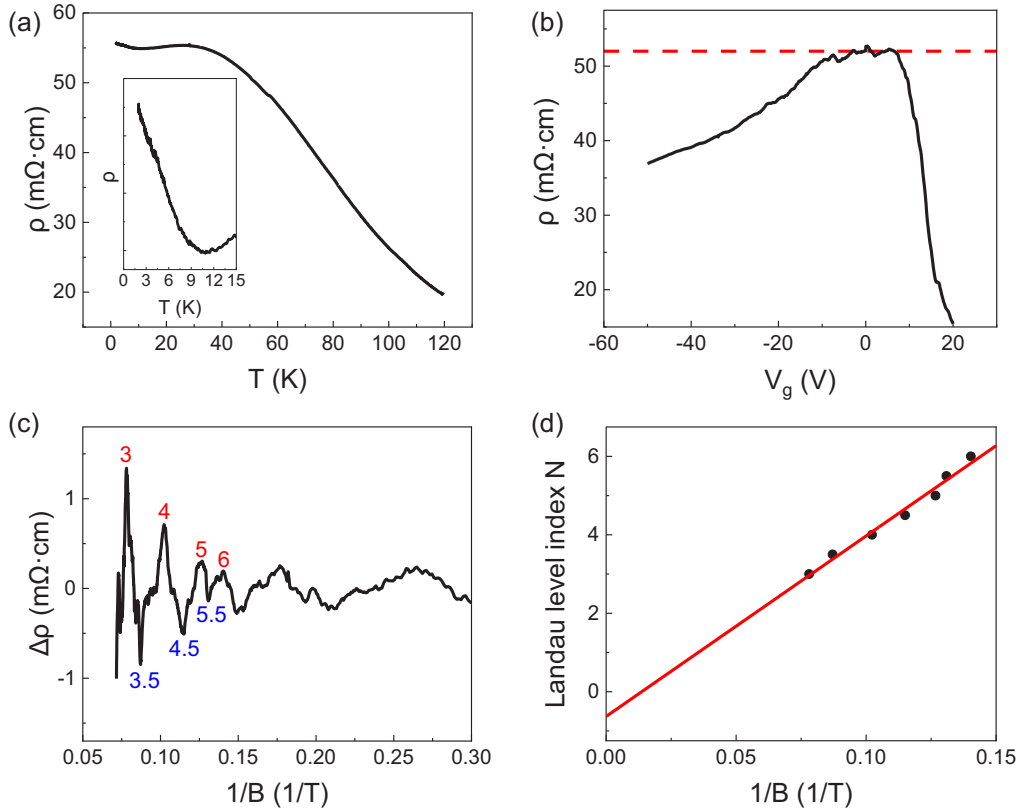


FIG. 3. Transport measurements on the bent region A1. (a) Measured resistivity ρ as a function of temperature T . Inset: Zoom-in view of ρ - T plot around 10 K. (b) Gate voltage dependence of resistivity. A flat region is observed between $V_g = -10$ and $+10$ V with a dashed guide-to-the-eye curve. (c) Shubnikov-de Haas (SdH) oscillations are observed. Landau levels are labeled with oscillation peaks being integers and oscillation valleys being half integers. (d) Landau level index N plotted against $1/B$. Peak and valley values obtained from SdH plot (c) are specified with black dots.

($1/B < 0.2 \text{ T}^{-1}$), allowing us to derive the Landau level index plot $N-1/B$, as shown in Fig. 3(d). Here, oscillation peaks correspond to integer indices and valleys to half-integer indices. An obvious linear relation in $N-1/B$ is clearly observable, and the intercept on the N axis is ~ -0.6 . A similar SdH oscillation and Landau fan diagram are also captured on the small strained region of other devices, e.g., device B (see Appendix C). It is worth noting that, according to the gate voltage dependence curve [Fig. 3(b)], the Fermi level of the system is situated within the bulk gap at zero gate. Therefore, the observed SdH oscillation pattern without gate modulation should not come from the formation of bulk Landau bands. A highly possible origin of the observed oscillation might be the topological surface states. Further, the obtained intercept -0.6 is close to the theoretical value $\pm \frac{1}{2}$ expected from topological insulator surface states [56–61], implying that the tendency of transition into topological insulator phase is happening in the bent nanoribbon sample. Actually, previous theoretical calculations [7,8,62] have predicted that, due to the inverted band structure, the Dirac semimetal Cd_3As_2 would be driven into a three-dimensional topological insulator under symmetry breakings. In our experiments, the applied bending strain serves as the symmetry-breaking factor and would break the C_4 rotational symmetry, rendering the presence of a topological insulator phase.

According to our general analysis of band evolution in the bent Cd_3As_2 nanoribbon system with large strain, local lattice deformation varies notably with respect to spatial position due to the inhomogeneous strain profile, making the band energy shift the dominant effect in this case. In previous literatures, there were similar reports concerning the drastic changes in band profiles caused by large strain in topological materials, for example, in the HgTe system [63,64]. In the complex system of the bent Cd_3As_2 nanoribbon here, it is reasonable to anticipate consecutive new transition of transport properties by further increasing the strain and exceeding the weak symmetry-breaking regime. To investigate the corresponding possibility, we performed transport measurements on a second region, noted as A2 [Fig. 4(a)], of the same nanoribbon sample, where strain was designed to be much more enhanced than region A1. In the bent region A2, the maximal strain is estimated to be $\varepsilon = 2.80\%$ with $r = 3.46 \mu\text{m}$ and $d = 194 \text{ nm}$, respectively.

Gate-voltage dependence of the resistivity in the largely bent nanoribbon region A2 was measured, as shown in Fig. 4(b). Interestingly, it is observed that the typical transfer curve of a gapless semimetallic system, featured with a single sharp resistivity peak, again emerges in the largely bent nanoribbon. From the transfer curve, we can obtain the carrier mobilities $\mu_e = 2.68 \times 10^4 \text{ cm}^2/(\text{V} \cdot \text{s})$ and $\mu_h = 7.32 \times 10^2 \text{ cm}^2/(\text{V} \cdot \text{s})$, much more enhanced than the weakly

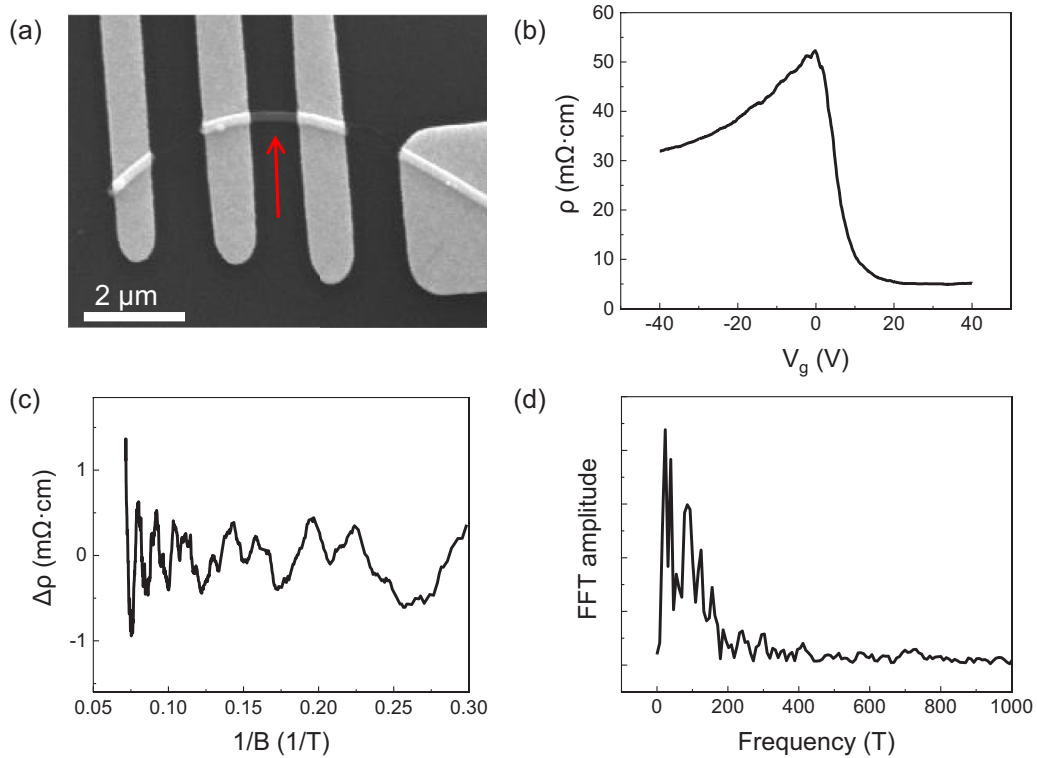


FIG. 4. Transport measurements on the largely bent region A2. (a) Scanning electron microscopy (SEM) image of the region A2 from the same nanoribbon as that in Fig. 2(a). The red arrow indicates the measurement region A2. The local curvature radius is $r = 3.46 \mu\text{m}$, corresponding to a maximal strain amplitude $\varepsilon = 2.80\%$. (b) Gate voltage dependence of resistivity. Single sharp peak feature typical for a semimetal is retrieved. (c) The resistivity oscillation $\Delta\rho$ after subtracting the background. (d) Fast Fourier transformation (FFT) spectrum of resistivity oscillation in (c).

bent case A1. Resistivity oscillations are also observed for the largely bent region, as shown in Fig. 4(c). The collective oscillation is a combination of multiple SdH oscillation patterns with different frequencies, as indicated by the fast Fourier transformation (FFT) spectrum in Fig. 4(d). The multiple-frequency oscillation pattern is also observed in the bent region A3 of the same nanoribbon, which has similar bending strength and strain gradient as those of region A2 (see Appendix B).

Within the framework of band evolution in the bent Cd_3As_2 nanoribbon as we proposed earlier [Figs. 2(c)–2(e)], the experimental results observed here can be well understood. First, the gapless Dirac semimetal feature seems to be retrieved in the gate-voltage modulation result [Fig. 4(b)]. This can be understood as follows. For simplicity, we regard the conduction in the nanoribbon as a parallel connection of two sample edges, as depicted in Fig. 2(e). When the Fermi level is raised by the gate, it will first touch the valence band top and then enter the energy gap on the outer side of the ribbon (lower-left panel), while the inner side of the ribbon still has the Fermi level crossing its valence band (lower-right panel). In this case, the conduction is dominated by the inner side of the ribbon, corresponding to p -type conduction. By further raising the Fermi energy, it will reach the conduction band bottom of the outer side in priority, then reach the valence band top on the inner side. In such a procedure, conversion from p to n type happens, which can be a very rapid change

analogous to a typical metallic system. By stepping further on raising the Fermi level, the inner side becomes insulating, while the outer side shows dominant n -type conductance. In the real nanoribbon system where infinite folds of the band configuration are parallelly connected, the main idea in our simplified model should still hold true and be applicable in explaining the obtained results. Then the resistivity oscillation in Fig. 4(c) can be explained in a similar manner as well. The conduction in the bent nanoribbon comprises contribution from multiple different lattice configurations with varying lattice constants and different band profiles. Since the Fermi level is equal everywhere in the sample, one can expect that the cross-sectional area of the “local Fermi surface” is also spatially dependent. Therefore, the observed resistivity oscillation in A2 and A3 is a superposition of many SdH oscillations with different frequencies, according to the Lifshitz-Onsager quantization rule [65]. The observation of a multifrequency SdH oscillation pattern thus also verifies the prominent band evolution induced by strong local strain effects, in accordance with the general comprehension proposed by us. The strain-mediated SdH oscillations are also observed in device C, where single-frequency SdH oscillation emerges in the weak strain regime and multi-frequency oscillation in the strong strain case (see Appendixes D and E). Notably, the Fermi level of the nanoribbon in device C is far away from the charge neutrality point, different from the case of devices A and B.

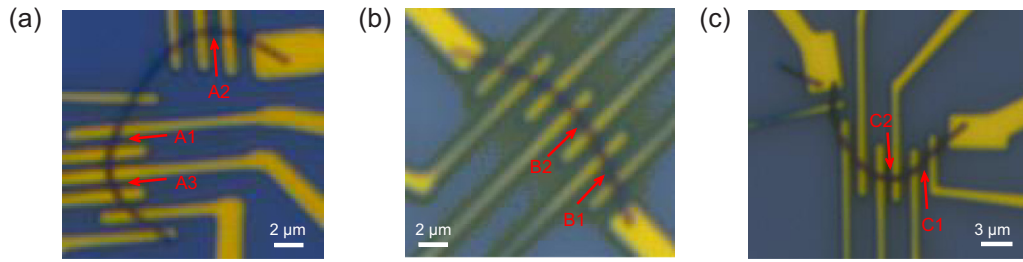


FIG. 5. Optical images of device A, B, and C, respectively. The red arrows denote the bent regions with different curvature radius for each device.

IV. CONCLUSIONS

In conclusion, we have performed a detailed investigation on the effect of the bending strain profile on the transport properties of a bent Dirac semimetal Cd_3As_2 nanoribbon. The introduced strain gradient would break the pristine lattice symmetry and result in the gap opening near the neutrality point. When further enhancing the strain strength, the gap gradually closes, which possibly originates from nonnegligible local strain effect that dominates over the symmetry-breaking effect. Our results demonstrate the strain-gradient induced topological phase transition in Dirac semimetals via transport methods. This approach to induce phase transition should be generic not only to Dirac semimetals but also to other topological materials.

ACKNOWLEDGMENT

This paper was supported by the National Natural Science Foundation of China (Grants No. 91964201, No. 61825401, and No. 11774004).

APPENDIX A: CHARACTERIZATION OF THE FINISHED BENT NANORIBBON DEVICES

Figure 5 shows the optical image of three typical devices, marked as device A, B, and C, respectively. The red arrows indicate the bent regions with different strain strength of the same nanoribbon sample. The thickness of selected nanoribbons ranges from 170 to 200 nm, which ensures the Dirac semimetal phase in unbent conditions. The local curvature

radius r , strain gradient g , and maximum strain amplitude ε of these bent regions are summarized in Table I. The value of the strain gradient is $g = 1/r$, and the maximal strain amplitude can be estimated as $\varepsilon = d/2r$, where d is the width of the nanoribbon.

APPENDIX B: TRANSPORT MEASUREMENTS ON ANOTHER BENT REGION OF DEVICE A

In device A, the bent region A3 has a similar curvature radius and maximal strain amplitude as those of region A2 described in Fig. 4. As expected, a multiple-frequency oscillation pattern [Figs. 6(b) and 6(c)] is observed in the region A3. Figure 6(a) displays the evolution of resistivity with varying temperature. In striking contrast to the case of bent region A1, the upturn <10 K is missing in the region A3. Instead, the resistivity exhibits a monotonic decay with decreasing the temperature <75 K. As seen from Fig. 2(e) in the main text, the large bending strain causes a prominent band shift through the nanoribbon, where no global band gap exists, and the sample Fermi level is always intersected with the energy bands. Thus, in this case, the insulating ρ - T behavior is absent in the low-temperature regime.

APPENDIX C: DIRAC SEMIMETAL PHASE IN THE RATHER WEAK STRAIN REGIME AND DOUBLE-FREQUENCY OSCILLATION PATTERN

Figure 7 demonstrates the transport results measured on device B. Upon weak bending strain, the resulting lattice

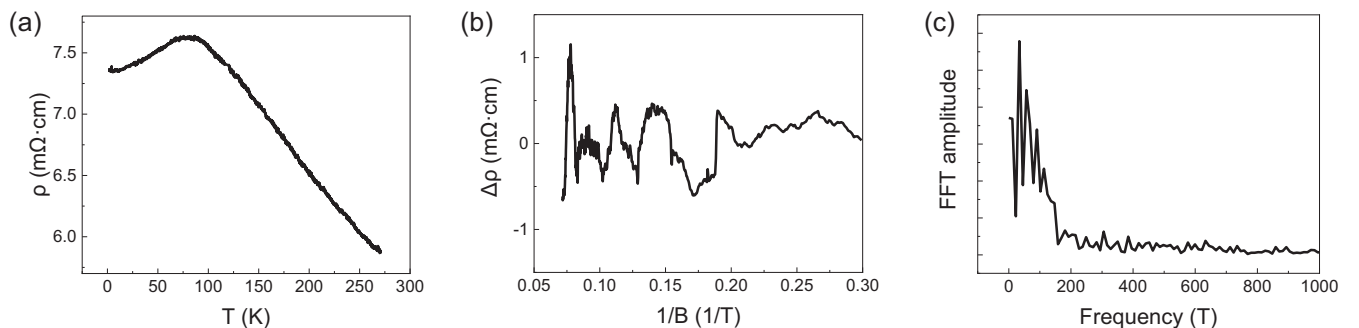


FIG. 6. Transport measurements on the largely bent region A3 ($r = 3.55 \mu\text{m}$, $\varepsilon = 2.75\%$). (a) Plot of resistivity ρ vs temperature T . (b) The resistivity oscillation $\Delta\rho$ as a function of the inverse of the magnetic field $1/B$. (c) Fast Fourier transformation (FFT) spectrum of resistivity oscillation in (b).

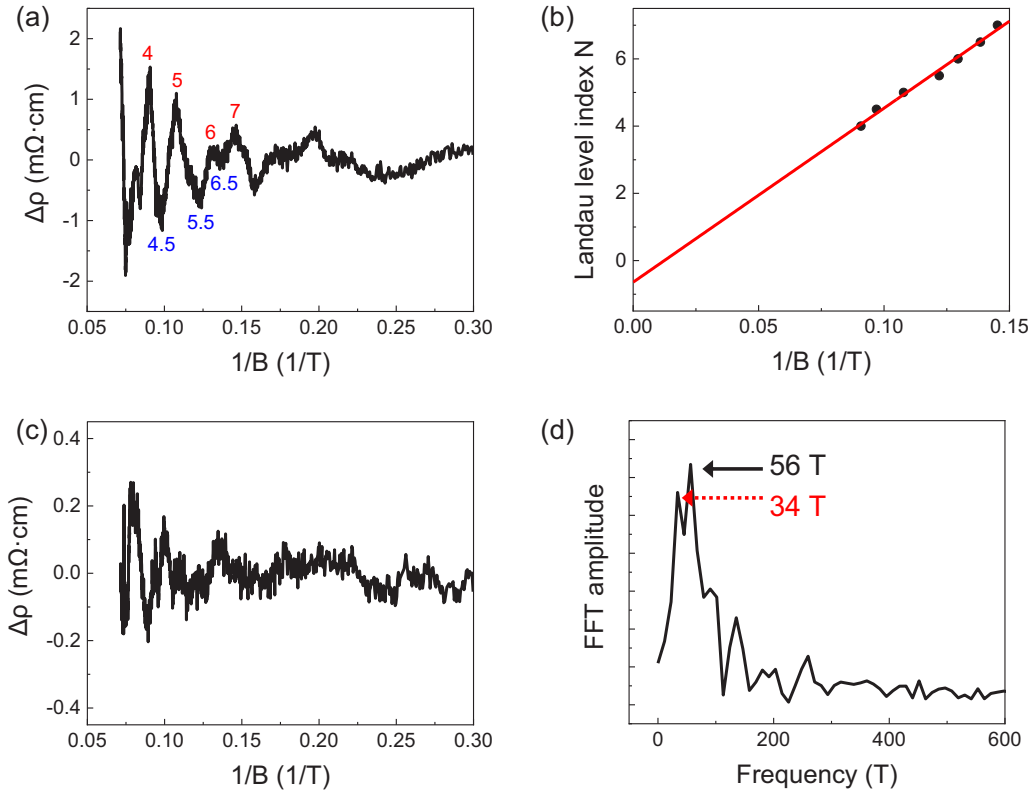


FIG. 7. Magnetotransport measurements on the nanoribbon device B. (a) Shubnikov–de Haas (SdH) oscillations in the weakly bent region B1 ($r = 25.5 \mu\text{m}$, $\varepsilon = 0.34\%$). Landau level indices are labeled with oscillation peaks being integers and valleys being half-integers. (b) Landau level fan diagram of SdH oscillations in (a). (c) The resistivity oscillations observed in the largely bent region B2 ($r = 8.98 \mu\text{m}$, $\varepsilon = 1.04\%$). (d) Fast Fourier transformation (FFT) spectrum of resistivity oscillation in (c).

deformation is almost negligible and would not open a bulk gap, where the Dirac semimetal phase is retained in the Cd_3As_2 nanoribbon. Figure 7(a) shows the SdH oscillations measured in the weakly bent region B1. The slope of the linear plot in the Landau level fan diagram gives the oscillation frequency of $\sim 52 \text{ T}$ [Fig. 7(b)]. The obtained intercept -0.64 is close to the theoretical value $-\frac{5}{8}$ expected in the Dirac semimetals [66]. Upon increasing the bending strain, the lattice deformation is gradually exacerbated, and finally, a band gap opens near the Dirac point. A resistivity oscillation pattern is also observed in the largely bent region B2, as shown in Fig. 7(c). Two peaks are found in the corresponding FFT spectrum [Fig. 7(d)]. The larger one ($\sim 56 \text{ T}$) is close to the value of the oscillation frequency captured in region B1, which should arise from the cyclotron motion of bulk carriers. The smaller one ($\sim 34 \text{ T}$) is most likely to originate from the surface states of the emergent insulator phase.

TABLE I. Geometric parameters of the nanoribbon devices.

Number region	Device A			Device B		Device C	
	A1	A2	A3	B1	B2	C1	C2
$r \text{ (}\mu\text{m)}$	4.13	3.46	3.55	25.50	8.98	11.68	2.68
$g \text{ (}\% \mu\text{m}^{-1}\text{)}$	24.2	28.9	28.2	3.9	11.1	8.6	37.3
$\varepsilon \text{ (}\% \text{)}$	2.41	2.80	2.75	0.34	1.04	0.83	3.08

APPENDIX D: DISCUSSION ABOUT STRAIN EFFECTS ON THE TRANSPORT PROPERTIES OF BULK-DOMINATED NANORIBBONS

Generally, the electronic transport properties are closely associated with the energy band structure and the carrier density (the location of the Fermi level) of the studied material. Figures 2(c)–2(e) and the related text describe the modulation of the bending strain on the transport properties when the nanoribbon Fermi level is situated near the charge neutrality point. Here, we make an analysis of the condition where the Fermi level is far away from the charge neutrality point [Fig. 8]. Under a magnetic field, the resistivity

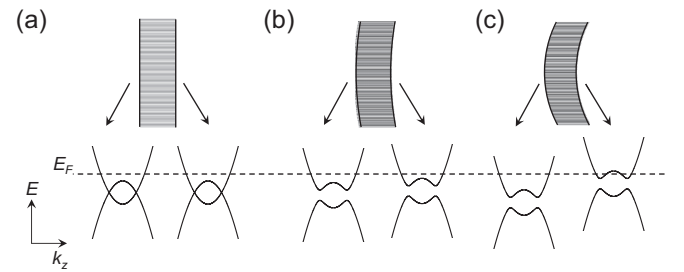


FIG. 8. Schematic of bulk band structure evolution in the bent Cd_3As_2 nanoribbon as the bending strength increases. Here, the Fermi level of nanoribbon is assumed to be situated highly above the charge neutrality point, distinct from the case of Figs. 2(c)–2(e).

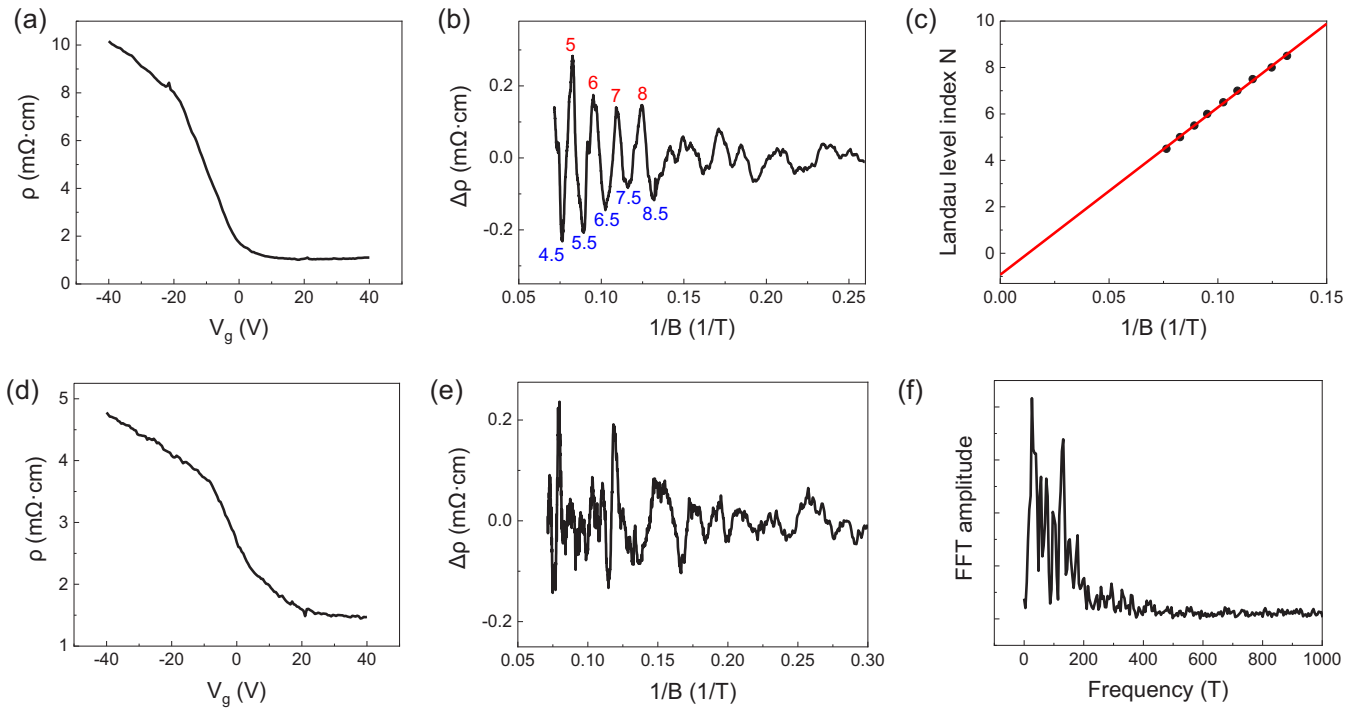


FIG. 9. Transport measurements on the nanoribbon device C. (a)–(c) correspond to the weakly bent region C1 ($r = 11.68 \mu\text{m}$, $\varepsilon = 0.83\%$), while (d)–(f) show the case of the strongly bent region C2 ($r = 2.68 \mu\text{m}$, $\varepsilon = 3.08\%$). (a) and (d) Transfer curves of the bent region C1 and C2, respectively. (b) Shubnikov–de Haas (SdH) oscillations in the region C1. Landau level indices are labeled with oscillation peaks being integers and valleys being half-integers. (c) Landau level fan diagram of SdH oscillations in (b). (e) Multiple-frequency resistivity oscillations observed in the region C2. (f) Fast Fourier transformation (FFT) spectrum of resistivity oscillation in (e).

oscillations would transform from a single-frequency to a multiple-frequency pattern with increasing the strain strength. The single-frequency corresponds to the cyclotron motion of bulk carriers, different from the case of Fig. 2(d), where surface states contribute to the single-frequency pattern. Distinct origins may lead to different intercepts in the Landau level fan plot.

APPENDIX E: STRAIN-MEDIATED OSCILLATION PATTERNS IN THE HEAVILY ELECTRON-DOPED NANORIBBON

Figure 9 shows the transport results measured on the bent nanoribbon device C. Seen from the transfer curve in Figs. 9(a) and 9(d), the nanoribbon is heavily electron doped, and the Fermi level should situate deeply in the conduction bands. SdH oscillations are clearly observed in the weakly

bent region [Fig. 9(b)], where oscillation peaks correspond to integer Landau level indices, and oscillation valleys correspond to half-integers. The slope of the Landau fan plot [Fig. 9(c)] shows the frequency of SdH oscillations, that is, $F = 72.06 \text{ T}$. The large oscillation frequency further confirms that the Fermi level is far away from the charge neutrality point in this nanoribbon. The intercept ~ 0.9 is consistent with the theoretical value of topological semimetal near the Lifshitz transition point [66]. This can be easily understood since the strain is not enough to open a bulk gap, where the Dirac semimetal phase is still maintained in region C1. The case is different when the applied bending strain is large. The local strain effect dominates and gives rise to a spatially dependent band shift [Fig. 8(c)]. Under a magnetic field, the cross-sectional area of the local Fermi surface is nonuniform through the nanoribbon. Thus, a multiple-frequency oscillation pattern is observed in the strongly bent region C2, as shown in Figs. 9(e) and 9(f).

[1] M. Z. Hasan and C. L. Kane, Colloquium: Topological insulators, *Rev. Mod. Phys.* **82**, 3045 (2010).
 [2] X.-L. Qi and S.-C. Zhang, Topological insulators and superconductors, *Rev. Mod. Phys.* **83**, 1057 (2011).
 [3] A. A. Burkov, Topological semimetals, *Nat. Mater.* **15**, 1145 (2016).
 [4] S. Wang, B.-C. Lin, A.-Q. Wang, D.-P. Yu, and Z.-M. Liao, Quantum transport in Dirac and Weyl semimetals: A review, *Adv. Phys.: X* **2**, 518 (2017).

[5] N. P. Armitage, E. J. Mele, and A. Vishwanath, Weyl and Dirac semimetals in three-dimensional solids, *Rev. Mod. Phys.* **90**, 015001 (2018).
 [6] A.-Q. Wang, X.-G. Ye, D.-P. Yu, and Z.-M. Liao, Topological semimetal nanostructures: from properties to topotronics, *ACS Nano* **14**, 3755 (2020).
 [7] B.-J. Yang and N. Nagaosa, Classification of stable three-dimensional Dirac semimetals with nontrivial topology, *Nat. Commun.* **5**, 4898 (2014).

- [8] Z. Wang, H. Weng, Q. Wu, X. Dai, and Z. Fang, Three-dimensional Dirac semimetal and quantum transport in Cd_3As_2 , *Phys. Rev. B* **88**, 125427 (2013).
- [9] M. Uchida, Y. Nakazawa, S. Nishihaya, K. Akiba, M. Kriener, Y. Kozuka, A. Miyake, Y. Taguchi, M. Tokunaga, N. Nagaosa *et al.*, Quantum Hall states observed in thin films of Dirac semimetal Cd_3As_2 , *Nat. Commun.* **8**, 2274 (2017).
- [10] C.-Z. Li, C. Li, L.-X. Wang, S. Wang, Z.-M. Liao, A. Brinkman, and D.-P. Yu, Bulk and surface states carried supercurrent in ballistic Nb-Dirac semimetal Cd_3As_2 nanowire-Nb junctions, *Phys. Rev. B* **97**, 115446 (2018).
- [11] C. Li, J. C. de Boer, B. de Ronde, S. V. Ramankutty, E. van Heumen, Y. Huang, A. de Visser, A. A. Golubov, M. S. Golden, and A. Brinkman, 4π -periodic Andreev bound states in a Dirac semimetal, *Nat. Mater.* **17**, 875 (2018).
- [12] A.-Q. Wang, C.-Z. Li, C. Li, Z.-M. Liao, A. Brinkman, and D.-P. Yu, 4π -Periodic Supercurrent from Surface States in Cd_3As_2 Nanowire-Based Josephson Junctions, *Phys. Rev. Lett.* **121**, 237701 (2018).
- [13] C.-Z. Li, A.-Q. Wang, C. Li, W.-Z. Zheng, A. Brinkman, D.-P. Yu, and Z.-M. Liao, Topological Transition of Superconductivity in Dirac Semimetal Nanowire Josephson Junctions, *Phys. Rev. Lett.* **126**, 027001 (2021).
- [14] C.-Z. Li, L.-X. Wang, H. Liu, J. Wang, Z.-M. Liao, and D.-P. Yu, Giant negative magnetoresistance induced by the chiral anomaly in individual Cd_3As_2 nanowires, *Nat. Commun.* **6**, 10137 (2015).
- [15] L.-X. Wang, C.-Z. Li, D.-P. Yu, and Z.-M. Liao, Aharonov-Bohm oscillations in Dirac semimetal Cd_3As_2 nanowires, *Nat. Commun.* **7**, 10769 (2016).
- [16] B.-C. Lin, S. Wang, L.-X. Wang, C.-Z. Li, J.-G. Li, D. Yu, and Z.-M. Liao, Gate-tuned Aharonov-Bohm interference of surface states in a quasiballistic Dirac semimetal nanowire, *Phys. Rev. B* **95**, 235436 (2017).
- [17] T. Schumann, L. Galletti, D. A. Kealhofer, H. Kim, M. Goyal, and S. Stemmer, Observation of the Quantum Hall Effect in Confined Films of the Three-Dimensional Dirac Semimetal Cd_3As_2 , *Phys. Rev. Lett.* **120**, 016801 (2018).
- [18] B.-C. Lin, S. Wang, S. Wiedmann, J.-M. Lu, W.-Z. Zheng, D. Yu, and Z.-M. Liao, Observation of an Odd-Integer Quantum Hall Effect from Topological Surface States in Cd_3As_2 , *Phys. Rev. Lett.* **122**, 036602 (2019).
- [19] B.-C. Lin, S. Wang, A.-Q. Wang, Y. Li, R.-R. Li, K. Xia, D. Yu, and Z.-M. Liao, Electric Control of Fermi Arc Spin Transport in Individual Topological Semimetal Nanowires, *Phys. Rev. Lett.* **124**, 116802 (2020).
- [20] A.-Q. Wang, P.-Z. Xiang, X.-G. Ye, W.-Z. Zheng, D. Yu, and Z.-M. Liao, Room-Temperature Manipulation of Spin Texture in a Dirac Semimetal, *Phys. Rev. Appl.* **14**, 054044 (2020).
- [21] A.-Q. Wang, P.-Z. Xiang, X.-G. Ye, W.-Z. Zheng, D. Yu, and Z.-M. Liao, Surface engineering of antisymmetric linear magnetoresistance and spin-polarized surface state transport in Dirac semimetals, *Nano Lett.* **21**, 2026 (2021).
- [22] E. V. Gorbar, V. A. Miransky, and I. A. Shovkovy, Engineering Weyl nodes in Dirac semimetals by a magnetic field, *Phys. Rev. B* **88**, 165105 (2013).
- [23] J. Cao, S. Liang, C. Zhang, Y. Liu, J. Huang, Z. Jin, Z. G. Chen, Z. Wang, Q. Wang, J. Zhao *et al.*, Landau level splitting in Cd_3As_2 under high magnetic fields, *Nat. Commun.* **6**, 7779 (2015).
- [24] H. Pan, M. Wu, Y. Liu, and S. A. Yang, Electric control of topological phase transitions in Dirac semimetal thin films, *Sci. Rep.* **5**, 14639 (2015).
- [25] S. Jeon, B. B. Zhou, A. Gyenis, B. E. Feldman, I. Kimchi, A. C. Potter, Q. D. Gibson, R. J. Cava, A. Vishwanath, and A. Yazdani, Landau quantization and quasiparticle interference in the three-dimensional Dirac semimetal Cd_3As_2 , *Nat. Mater.* **13**, 851 (2014).
- [26] W.-Z. Zheng, X.-G. Ye, B.-C. Lin, R.-R. Li, D.-P. Yu, and Z.-M. Liao, Magnetotransport evidence for topological phase transition in a Dirac semimetal, *Appl. Phys. Lett.* **115**, 183103 (2019).
- [27] A. Cortijo, Y. Ferreira, K. Landsteiner, and M. A. Vozmediano, Elastic Gauge Fields in Weyl Semimetals, *Phys. Rev. Lett.* **115**, 177202 (2015).
- [28] R. Ilan, A. G. Grushin, and D. I. Pikulin, Pseudo-electromagnetic fields in 3D topological semimetals, *Nat. Rev. Phys.* **2**, 29 (2019).
- [29] T. Liu, D. I. Pikulin, and M. Franz, Quantum oscillations without magnetic field, *Phys. Rev. B* **95**, 041201(R) (2017).
- [30] N. Levy, S. A. Burke, K. L. Meaker, M. Panlasigui, A. Zettl, F. Guinea, A. H. C. Neto, and M. F. Crommie, Strain-induced pseudo-magnetic fields greater than 300 Tesla in graphene nanobubbles, *Science* **329**, 544 (2010).
- [31] D. I. Pikulin, A. Chen, and M. Franz, Chiral Anomaly from Strain-Induced Gauge Fields in Dirac and Weyl Semimetals, *Phys. Rev. X* **6**, 041021 (2016).
- [32] A. G. Grushin, J. W. F. Venderbos, A. Vishwanath, and R. Ilan, Inhomogeneous Weyl and Dirac Semimetals: Transport in Axial Magnetic Fields and Fermi Arc Surface States from Pseudo-Landau Levels, *Phys. Rev. X* **6**, 041046 (2016).
- [33] H. Sumiyoshi and S. Fujimoto, Torsional Chiral Magnetic Effect in a Weyl Semimetal with a Topological Defect, *Phys. Rev. Lett.* **116**, 166601 (2016).
- [34] H. Shapourian, T. L. Hughes, and S. Ryu, Viscoelastic response of topological tight-binding models in two and three dimensions, *Phys. Rev. B* **92**, 165131 (2015).
- [35] C. Z. Li, J. G. Li, L. X. Wang, L. Zhang, J. M. Zhang, D. Yu, and Z. M. Liao, Two-carrier transport induced hall anomaly and large tunable magnetoresistance in dirac semimetal Cd_3As_2 nanoplates, *ACS Nano* **10**, 6020 (2016).
- [36] T. N. Pardue, M. Goyal, B. Guo, S. Salmani-Rezaie, H. Kim, O. Heinonen, M. D. Johannes, and S. Stemmer, Controlling the symmetry of cadmium arsenide films by epitaxial strain, *APL Mater.* **9**, 051111 (2021).
- [37] P. Villar Arribi, J.-X. Zhu, T. Schumann, S. Stemmer, A. A. Burkov, and O. Heinonen, Topological surface states in strained Dirac semimetal thin films, *Phys. Rev. B* **102**, 155141 (2020).
- [38] X. Yuan, P. Cheng, L. Zhang, C. Zhang, J. Wang, Y. Liu, Q. Sun, P. Zhou, D. W. Zhang, Z. Hu *et al.*, Direct observation of Landau level resonance and mass generation in Dirac semimetal Cd_3As_2 thin films, *Nano Lett.* **17**, 2211 (2017).
- [39] J. Feng, Y. Pang, D. Wu, Z. Wang, H. Weng, J. Li, X. Dai, Z. Fang, Y. Shi, and L. Lu, Large linear magnetoresistance in Dirac semimetal Cd_3As_2 with Fermi surfaces close to the Dirac points, *Phys. Rev. B* **92**, 081306 (2015).
- [40] H. Chi, C. Zhang, G. Gu, D. E. Kharzeev, X. Dai, and Q. Li, Lifshitz transition mediated electronic transport anomaly in bulk ZrTe_5 , *New J. Phys.* **19**, 015005 (2017).

- [41] S. Anissimova, S. V. Kravchenko, A. Punnoose, A. M. Finkel'stein, and T. M. Klapwijk, Flow diagram of the metal-insulator transition in two dimensions, *Nat. Phys.* **3**, 707 (2007).
- [42] L. Craco, M. S. Laad, and S. Leoni, Low-temperature metal-insulator transition in the electron-doped iron chalcogenide FeSe superconductor, *Europhys. Lett.* **91**, 27001 (2010).
- [43] E. Janod, J. Tranchant, B. Corraze, M. Querré, P. Stoliar, M. Rozenberg, T. Cren, D. Roditchev, V. T. Phuoc, M.-P. Besland *et al.*, Resistive switching in Mott insulators and correlated systems, *Adv. Funct. Mater.* **25**, 6287 (2015).
- [44] X. Shen, X. Qiu, D. Su, S. Zhou, A. Li, and D. Wu, Thickness-dependent metal-insulator transition in epitaxial SrRuO₃ ultrathin films, *J. Appl. Phys.* **117**, 015307 (2015).
- [45] S. Zhang, Q. Wu, L. Schoop, M. N. Ali, Y. Shi, N. Ni, Q. Gibson, S. Jiang, V. Sidorov, W. Yi *et al.*, Breakdown of three-dimensional Dirac semimetal state in pressurized Cd₃As₂, *Phys. Rev. B* **91**, 165133 (2015).
- [46] C. Zhang, J. Sun, F. Liu, A. Narayan, N. Li, X. Yuan, Y. Liu, J. Dai, Y. Long, Y. Uwatoko *et al.*, Evidence for pressure-induced node-pair annihilation in Cd₃As₂, *Phys. Rev. B* **96**, 155205 (2017).
- [47] A. A. Shashkin and S. V. Kravchenko, Recent developments in the field of the metal-insulator transition in two dimensions, *Appl. Sci.* **9**, 1169 (2019).
- [48] L. X. Wang, S. Wang, J. G. Li, C. Z. Li, J. Xu, D. Yu, and Z. M. Liao, Magnetotransport properties near the Dirac point of Dirac semimetal Cd₃As₂ nanowires, *J. Phys.: Condens. Matter* **29**, 044003 (2017).
- [49] M. König, S. Wiedmann, C. Brüne, A. Roth, H. Buhmann, L. W. Molenkamp, X.-L. Qi, and S.-C. Zhang, Quantum spin Hall insulator state in HgTe quantum wells, *Science* **318**, 766 (2007).
- [50] S. Wu, V. Fatemi, Q. D. Gibson, K. Watanabe, T. Taniguchi, R. J. Cava, and P. Jarillo-Herrero, Observation of the quantum spin Hall effect up to 100 Kelvin in a monolayer crystal, *Science* **359**, 76 (2018).
- [51] C. Liu, Y. Wang, H. Li, Y. Wu, Y. Li, J. Li, K. He, Y. Xu, J. Zhang, and Y. Wang, Robust axion insulator and Chern insulator phases in a two-dimensional antiferromagnetic topological insulator, *Nat. Mater.* **19**, 522 (2020).
- [52] H. Steinberg, D. R. Gardner, Y. S. Lee, and P. Jarillo-Herrero, Surface state transport and ambipolar electric field effect in Bi₂Se₃ nanodevices, *Nano Lett.* **10**, 5032 (2010).
- [53] J. G. Checkelsky, Y. S. Hor, R. J. Cava, and N. P. Ong, Bulk Band Gap and Surface State Conduction Observed in Voltage-Tuned Crystals of the Topological Insulator Bi₂Se₃, *Phys. Rev. Lett.* **106**, 196801 (2011).
- [54] E. Xypakis and J. H. Bardarson, Conductance fluctuations and disorder induced $\nu = 0$ quantum Hall plateau in topological insulator nanowires, *Phys. Rev. B* **95**, 035415 (2017).
- [55] M. Neupane, S. Y. Xu, R. Sankar, N. Alidoust, G. Bian, C. Liu, I. Belopolski, T. R. Chang, H. T. Jeng, H. Lin *et al.*, Observation of a three-dimensional topological Dirac semimetal phase in high-mobility Cd₃As₂, *Nat. Commun.* **5**, 3786 (2014).
- [56] M. V. Berry, Quantal phase factors accompanying adiabatic changes, *Proc. Math. Phys. Eng. Sci.* **392**, 45 (1984).
- [57] G. P. Mikitik and Y. V. Sharlai, Manifestation of Berry's Phase in Metal Physics, *Phys. Rev. Lett.* **82**, 2147 (1999).
- [58] D. Xiao, M.-C. Chang, and Q. Niu, Berry phase effects on electronic properties, *Rev. Mod. Phys.* **82**, 1959 (2010).
- [59] Y. Yan, Z.-M. Liao, Y.-B. Zhou, H.-C. Wu, Y.-Q. Bie, J.-J. Chen, J. Meng, X.-S. Wu, and D.-P. Yu, Synthesis and quantum transport properties of Bi₂Se₃ topological insulator nanostructures, *Sci. Rep.* **3**, 1264 (2013).
- [60] L. Fang, Y. Jia, D. J. Miller, M. L. Latimer, Z. L. Xiao, U. Welp, G. W. Crabtree, and W. K. Kwok, Catalyst-free growth of millimeter-long topological insulator Bi₂Se₃ nanoribbons and the observation of the π -Berry phase, *Nano Lett.* **12**, 6164 (2012).
- [61] W. Zhao, L. Chen, Z. Yue, Z. Li, D. Cortie, M. Fuhrer, and X. Wang, Quantum oscillations of robust topological surface states up to 50 K in thick bulk-insulating topological insulator, *npj Quantum Mater.* **4**, 56 (2019).
- [62] A. Rancati, N. Pournaghavi, M. F. Islam, A. Debernardi, and C. M. Canali, Impurity-induced topological phase transitions in Cd₃As₂ and Na₃Bi Dirac semimetals, *Phys. Rev. B* **102**, 195110 (2020).
- [63] P. Leubner, L. Lunczer, C. Brune, H. Buhmann, and L. W. Molenkamp, Strain Engineering of the Band Gap of HgTe Quantum Wells Using Superlattice Virtual Substrates, *Phys. Rev. Lett.* **117**, 086403 (2016).
- [64] F. Kirtschig, J. van den Brink, and C. Ortix, Surface-state spin textures in strained bulk HgTe: strain-induced topological phase transitions, *Phys. Rev. B* **94**, 235437 (2016).
- [65] H. Murakawa, M. S. Bahramy, M. Tokunaga, Y. Kohama, C. Bell, Y. Kaneko, N. Nagaosa, H. Y. Hwang, and Y. Tokura, Detection of Berry's phase in a bulk Rashba semiconductor, *Science* **342**, 1490 (2013).
- [66] C. M. Wang, H.-Z. Lu, and S.-Q. Shen, Anomalous Phase Shift of Quantum Oscillations in 3D Topological Semimetals, *Phys. Rev. Lett.* **117**, 077201 (2016).